TUDelft

Delft University of Technology

Design of Integrated Hybrid Configuration of Modular Multilevel Converter and Marx Generator to Generate Complex Waveforms for Dielectric Testing of Grid Assets

Ganeshpure, Dhanashree ; Soeiro, Thiago Batista; Ghaffarian Niasar, Mohamad ; Kulkarni, Nitish Milind; Bauer, Pavol; Vaessen, Peter

Important note
To cite this publication, please use the final published version (if applicable).
Please check the document version above.

Design of Integrated Hybrid Configuration of Modular Multilevel Converter and Marx Generator to Generate Complex Waveforms for Dielectric Testing of Grid Assets

DHANASHREE ASHOK GANESHPURE [1] (Member, IEEE), THIAGO BATISTA SOEIRO [2] (Senior Member, IEEE),
MOHAMAD GHAFFARIAN NIASAR [1] (Member, IEEE), NITISH MILIND KULKARNI [1],
PAVOL BAUER [1] (Senior Member, IEEE), AND PETER VAESSEN [1,3] (Member, IEEE)

[1]Department of Electrical Sustainable Energy, Delft University of Technology, 2628 CD Delft, The Netherlands
[2]University of Twente, 7522 NB Enschede, The Netherlands
[3]KEMA Laboratories, 6812 DE Arnhem, The Netherlands

CORRESPONDING AUTHOR: MOHAMAD GHAFFARIAN NIASAR (e-mail: m.ghaffarianniasar@tudelft.nl).

ABSTRACT This article proposes a new configuration of a modular multilevel converter (MMC) and a Marx generator to generate fast-rising impulse waveforms. This new configuration improves the capabilities of the MMC-based high voltage arbitrary wave shape generator to generate fast-rising impulse since the MMC topology faces many inherent limitations. Similar to the conventional superimposed circuit of the ac transformer or dc rectifier circuit with the Marx generator, three hybrid circuits of MMC and the Marx generator are introduced, where the most optimal choice is made considering the practical aspects of testing, such as the size, cost, and preparation time. Then, a detailed analytical study is performed on the Marx generator circuit and the MMC circuit, and both circuits are coupled together to deliver a complete guideline on choosing various system parameters when the impulse wave shape and the load capacitor are given. The concept of this new hybrid configuration is demonstrated with a scaled-down prototype where the impulse with a rise time of 1 μs is superimposed on different arbitrary wave shapes. Similarly, the MATLAB-Simulink simulation model validates the proposed configuration for a 200 kV dc link voltage and 67 submodules with the desired impulse performance.

INDEX TERMS Lightning impulse, Marx generator, modular multilevel converter (MMC), superimposed waveforms.

I. INTRODUCTION

Medium voltage (MV) and high voltage (HV) equipment such as transformers, switchgear, and cables in the electrical power system are experiencing new and more severe electrical stresses due to the rise of distributed generation (DG) systems and large-scale renewable energy integration by power electronic converters [1], [2], [3], [4]. For the reliable operation of current and future electrical power systems, MV and HV equipment needs to be tested with electric stresses with complex wave shapes, as shown in Fig. 1(a) and (b). Since these wave shapes are complicated to generate with the existing HV test sources, their equivalent waveforms are formulated as the superimposition of impulse on ac or dc waveforms, as shown in Fig. 1(c) and (d). These superimposed waveforms can be generated using the existing HV test sources in the circuit, as shown in Fig. 2 [5].

The left side of Fig. 2 can be either a transformer or a rectifier circuit to generate the ac or dc part of the complex voltage waveforms. The Marx generator, which can generate impulse waveforms with various rise and tail times, is shown on the right side of the figure. Typically, in dielectric testing, two standardized impulse waveforms are used. The first one is

FIGURE 1. Typical complex voltage waveforms required for the dielectric tests of grid assets [2], [3], [4], [5].

FIGURE 2. Test circuit for generating superimposed waveforms shown in Fig. 1 [5].

FIGURE 3. (a) Schematic of the MMC-based HV AWG. (b) Equivalent circuit of MMC for LI operation.

FIGURE 4. LI voltage waveform and the required current provided by the MMC.

a lightning impulse (LI) with a rise time of 1.2 µs and tail time of 50 µs, and the second one is a switching impulse (SI) with a rise time of 250 µs and tail time of 2500 µs [6]. Fig. 1(a) and (b) shows waveforms with the superposition of a SI [3], [4] and Fig. 1(c) and (d) shows waveforms with the superposition of a LI on a 50 Hz ac and dc, respectively [5].

Complex waveforms illustrated in Fig. 1(a) and (b) cannot be generated from the above-mentioned superimposed waveform generation circuit since it is not possible to program conventional equipment such as a transformer and rectifier. Hence, many HV researchers are designing new test circuits to address the need for an HV test source with high bandwidth and sufficient current capability [3], [2], [7], [8]. A modular multilevel converter (MMC)-based arbitrary wave shape generator (AWG) is proposed in [4], which can generate such complex waveforms by itself with a designed value of the bandwidth and with the possibility to scale up the voltage and current comparatively quickly. The schematic of such an MMC-based HV AWG is shown in Fig. 3(a).

The MV and HV equipment behaves electrically as capacitance, as shown in Fig. 3 and the typical range of this capacitance for MV equipment is from 50 pF to 10 nF [9]. The worst-case scenario for generating an LI waveform from an MMC-based HV AWG is the MV transformer with 36 kV voltage rating. The typical load capacitance of a 36 kV transformer is 10 nF and the required peak magnitude of LI is 250 kV. The MMC-based AWG must supply a pulse current

with a large magnitude and a very fast rise time to generate such a fast voltage waveform across such a large capacitive load. Fig. 3(b) is used for estimating the peak pulse current, and Fig. 4 shows the front side of the LI waveform and the current flowing through the switches of the MMC.

The switches in the MMC need to withstand pulse current magnitudes of 1.7 kA, and the rise time of this current needs to be 0.2 µs. Though kilo-amperes-rated insulated-gate bipolar transistors (IGBTs) and integrated gate-commutated thyristor (IGCTs) are available in the market, they will make the MMC-based HV AWG bulky and costly. Additionally, high-current switches are unsuitable since most of the other required dielectric tests require and would demand the MMC to generate a current in the range of a few amperes. Apart from the HV dielectric testing application, such a pulsed power operation of SM devices is extensively used in plasma applications [10]. Mostly, these plasma applications have a resistive load at a much lower voltage level. Even when it has a capacitive load, the capacitance is in the range of 150–600 pF [11]. Hence, the current requirements for these AWG are not as stringent as HV AWG application.

Many literature studies of discrete switches have shown that they can withstand much higher pulse current than the data sheet values [10], [11], [12], [13]. Considering the short duration of the pulse current in the LI waveform, the pulse current capability of different discrete switches is investigated to see if any of them satisfy the stringent pulse current requirement as explained above, and it is concluded that all

tested devices cannot satisfy the current requirement unless multiple switches are connected in parallel, resulting the design to be more complex and expensive [14]. Besides the peak pulse current magnitude, limiting the stray inductance in the series-connected MMC topology is extremely difficult, making it very complicated to generate the LI waveform by an MMC [10]. Hence, it is necessary to use the traditional Marx generator circuit to generate fast-rising impulses like LI. The idea of coupling the MMC and Marx generator is discussed in [15] for generating arbitrary wave shapes with rise times faster than 100 μs across the HVdc valves. However, it did not discuss different configurations or go into details about the interaction of the two circuits in analytical detail. Hence, the main contribution of this article is as follows.

1) Comparison of different possible solutions to integrate the traditional Marx generator circuit with the MMC-based HV AWG to generate complex wave shapes, which includes short impulses such as the LI waveform.
2) An exhaustive quantitative analysis of the design guideline for realizing such a hybrid configuration of two circuits, where an inherent interaction between the MMC-branch and the Marx generator circuit is discovered, which limits the capability of impulse generation.
3) Demonstration of the feasibility of the selected hybrid circuit with the scaled-down experimental prototype.
4) Verification of performance of this integrated hybrid configuration at full-scale HV level with a MATLAB-Simulink simulation model.

The rest of this article is organized as follows. Section II goes in-depth about the HV AWG application and clarifies the design requirement for the hybrid configuration of the MMC and Marx generator. Later, three possible hybrid configurations are compared in Section III, where the most optimal one is chosen to generate complex wave shapes. Next, Section IV analyzes different design tradeoffs to select system parameters for optimal performance of the hybrid circuit. Here, an important interaction between the MMC and Marx generator is observed, which can limit the impulses for different rise and tail times. The performance of the design is demonstrated with a scaled-down prototype with two submodules per arm in Section V. Additionally, the HV design of the integrated hybrid configuration is verified with MATLAB-Simulink simulations in Section VI. Finally, Section VII concludes this article.

II. FUNDAMENTALS OF HV TESTING APPLICATION

Before integrating the power grid equipment into the grid, they are tested to determine the mechanical, thermal, and dielectric properties for reliable operation. HV tests are used to determine the dielectric properties such as the dielectric strength, partial discharges, and dielectric losses of MV and HV insulation materials [16]. Power grid HV equipment and their HV testing have a long history of more than one century [17]. Organizations such as IEC and IEEE standardize these test procedures for particular voltage classes. As per the standard [18], MV equipment has operating voltages of
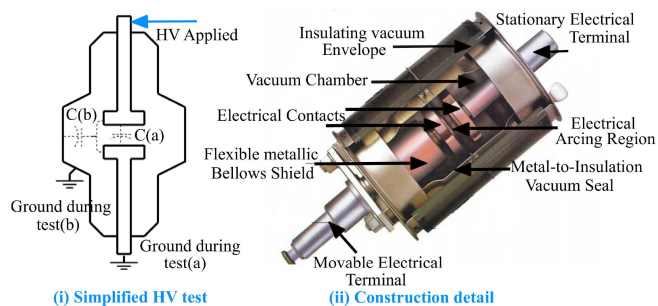

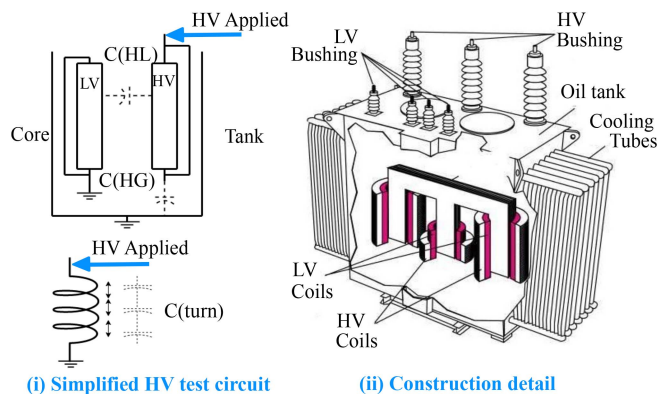**FIGURE 5.** MV vacuum circuit breaker [22].

FIGURE 6. MV distribution Transformer [23].

1–36 kV, and they need to be tested for higher voltage such as 100 kV for sinusoidal waveform and 250 kV for LI. The HV equipment ranges from 36 to 150 kV and needs extra-HV levels for the test.

Figs. 5–9 show pictures of the most commonly certified MV power grid equipment, i.e., circuit breaker, distribution transformer, cable, and instrument transformer. Instrument transformers can be of two types, i.e., potential transformer (PT) and current transformer (CT). These figures show the construction details of the equipment mentioned above with simplified diagrams of how HV tests are performed, especially about the applied HV potential and grounding parts. Additionally, the equivalent dielectric capacitances affecting the tests are shown. There is a significant difference between a distribution transformer and an instrument transformer (PT and CT both) regarding its construction and operation [19]. Hence, the dielectric tests performed on the distribution transformer and PT are different in their test circuit, as shown in Figs. 6 and 8. Though the test connections are the same for the distribution transformer and CT, there is only a single turn in the primary winding of a CT with a toroidal core [20] instead of a standard E core in the distribution transformer [21].

The capacitance range for the previously mentioned equipment is given in Table 1. In the EU, these MV equipments are tested according to the IEC standards [26], [27]. These tests consist mainly of sinusoidal and LI test waveforms [6]. Here,
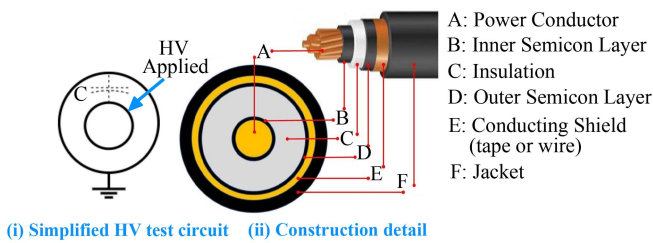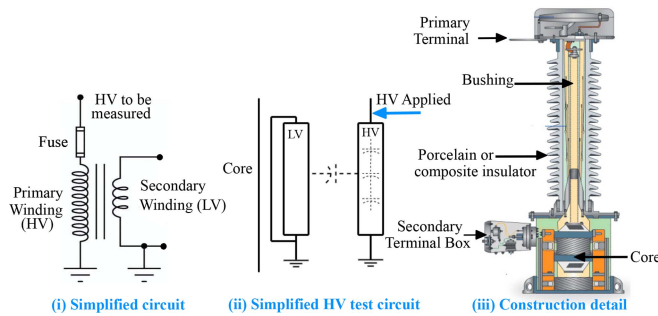
FIGURE 7. MV ac cable [24].

A: Power Conductor
B: Inner Semicon Layer
C: Insulation
D: Outer Semicon Layer
E: Conducting Shield
(tape or wire)
F: Jacket

(i) Simplified HV test circuit   (ii) Construction detail

FIGURE 8. MV potential transformer [25].

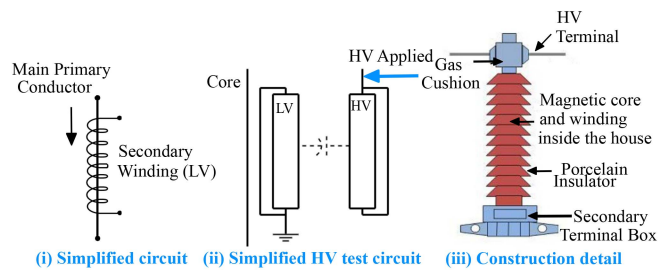(i) Simplified circuit   (ii) Simplified HV test circuit   (iii) Construction detail

FIGURE 9. MV current transformer [20].

TABLE 1. Typical Range of the Equivalent Capacitance of Dielectric Insulation Materials

Vacuum Circuit Breaker [9]	Distribution Transformer [9]	AC Cable [30]	Instrument Transformer [31]
C(a)=50 pF	C(HG)=12-16 nF	C=1-10 nF	C(PT)=1 nF
C(b)=50 pF	C(LG)=19-26 nF	length=10 m	C(CT)=0.25 nF

the sinusoidal waveform has 50 or 60 Hz grid frequency, and the LI is a steep impulse, as described in the introduction. The power frequency tests of MV class equipment are conducted at a higher voltage than the rated voltage of the equipment due to the different switching transients [16]. For example, a 3 kV equipment will be tested at 10 kV, and a 36 kV rated equipment is tested at 70–80 kV [28]. In some cases, the manufacturer or owner of the device under test (DUT) can customize a test that demands a higher voltage than the standardized value to test the limits of their equipment.

Similarly, the LI is tested at 6 to 7 times higher voltage than the rated voltage of the equipment, depending on the voltage class of the equipment. For example, a 36 kV transformer will

be tested with 170–220 kV LI [28]. Considering the margin in the HV requirement, the choice of 100 and 250 kV is done for the periodic waveforms and impulse waveforms, respectively. Hence, the LI waveform shown in Fig. 4 has a peak amplitude of 250 kV. Here, it is important to highlight that both positive and negative polarity LI needs to be applied to the HV equipment, and the test sequences for the particular equipment are given in their respective IEC standard such as [18], [26], [27], and [29].

Similar to the MV equipment, HV equipment is tested with power frequency and LI, with much higher voltage amplitudes. Additionally, HV equipment needs to be tested with the SI waveform and superimposed waveforms, as shown in Fig. 1(c) and (d). As mentioned, these two superimposed waveforms are simplified equivalents of other transients in the ac and dc grids. Generally, the transient happens while the HV components work at their rated voltage. Hence, the transient voltage gets added to the ac or dc voltage. It significantly affects the insulation strength of the HV equipment when subjected to the waveforms shown above. The first waveform in Fig. 1(a) is a transient waveform experienced by the 380 kV rated cable when a circuit breaker is operated in one of the sections of the Dutch transmission network [32].

Additionally, the HVdc cable in a symmetric monopole HVdc system needs to withstand transient for a few tens of milliseconds since the dc side circuit breaker is not present [4] and the resulted transient is shown in Fig. 1(b). In this figure, the base voltage is 350 or 550 kV. Both these complex waveforms are SI-based with a dominant frequency of a few kHz. It is important to highlight that the effect of SI waveform is more severe in HV equipment compared to LI, considering they are more frequent and severe in their effect on the insulation [3], [33]. SIs can stress insulation materials differently from lightning, potentially causing localized stress concentrations and insulation breakdown [34], [35]. As voltage levels increase, standards evolve to reflect HV equipment's specific challenges and requirements [5]. However, MV equipment is tested with only LI rather than both (LI & SI) waveforms since the LI waveform affects the insulation more severely. Hence, it is important to include the LI capability in the MMC-based HV AWG to test the worst-case scenario and understand the effect of such a steep pulse on the HV insulation, as studied in [3] and [5].

Apart from these equipment test levels, it is important to test the insulation material properties as the frequency injecting into the grid is increasing significantly [36], [37], [37], [38]. Hence, the capability of generating LI and other short impulses from the MMC-based HV AWG can be added by integrating it with the traditional Marx generator circuit. Impulses with a rise time of more than 100 μs can be directly generated from the MMC-based HV AWG, including SI. Considering the arm current flowing through the switches during steep rising impulses, this limit is set. However, when the rise time is increased from 1.2 to 100 μs, the current peak shown in Fig. 4 is reduced 100 times. With the current peak reduced to roughly around 17 A, discrete switches with 5–9 A can be
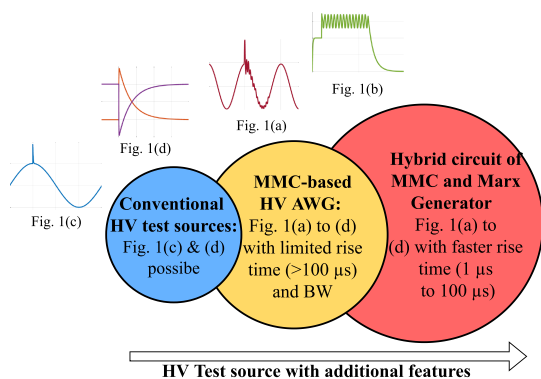
FIGURE 10. Summary of additional capabilities offered by the MMC-based HV AWG.

chosen since they can withstand 2–3 times higher current than rated values [14]. Fig. 10 summarizes the additional capabilities offered by this new HV test source compared to the conventional HV test source circuit.

The traditional superimposed circuit in Fig. 2 from the IEC-62895 standard [5] can add an impulse waveform on a sinusoidal or dc waveform. However, the MMC-based HV AWG can generate other high-frequency harmonics in the transient voltage stresses experienced by different HV equipment with the limited rise time possible. The integrated hybrid circuit combines the capability of an MMC-based HV AWG and a Marx generator, making shorter impulses like LI possible. This article focuses on the hybrid circuit design and generation of the complex wave shapes from Fig. 1(a) and (b) with LI and the two conventional test waveforms shown in Fig. 1(c) and (d). Though the HV equipment experiences these superimposed waveforms, the capability of the MMC-based AWG is showcased with 100 kV output voltage in the MATLAB-Simulink simulation with the largest load capacitance of 10 nF.

III. SCHEMATICS OF DIFFERENT HYBRID CONFIGURATIONS
Fig. 2 shows the IEC-recommended circuit for generating the superimposed waveforms. Similarly, the MMC and Marx generator circuits can be connected in parallel across the load capacitor, as shown in Fig. 11(a). It includes the complete schematic of the MMC-based HV AWG and a single stage of the impulse generator. Additionally, some coupling elements are necessary to protect two different circuits from each other. From the schematic of this hybrid circuit, it is clear that both test sources need capacitor-based dc input sources. Considering the high cost and large size of the HVdc source and the HV capacitors, two possible integrated hybrid circuits are proposed in Fig. 11(b) and 11(c). In these proposed schematics, the dc input side of the Marx generator and the MMC-based AWG are combined. An added benefit of the proposed circuit is the reduced preparation time for the superimposed test. It removes the need to move different equipment and test

objects from one lab section to another, which can be crucial in commercial testing.

The two proposed integrated hybrid circuits are quite similar, except Fig. 11(c) has an additional capacitor (C_s). From the basic understanding of the Marx generator circuit, the input capacitor gets entirely discharged into the test object [16]. It means that the dc link capacitance (C_{dc}) from Fig. 11(b) will be discharged after one impulse, which is not suitable for the proper operation of the MMC-based HV AWG. Hence, Fig. 11(c) has an additional capacitor C_s, which does not allow the C_{dc} capacitor discharge during the impulses by charging up the C_s capacitor negatively. This means that the voltage combined from C_{dc} and C_s will be zero, keeping the working principle of the Marx generator circuit intact. The following section outlines the design guidelines for the third circuit. It is essential to highlight that the design of the hybrid circuit in Fig. 11(a) and (c) is the same except for the additional design requirement for the dc side for the later circuit.

IV. DESIGN GUIDELINES
Though the design guidelines of the MMC-based HV AWG and Marx generator are known, the two test circuits are coupled with each other using two coupling elements. The first one is the parallel resistor (R_p) connected just before the load capacitor, and it protects the HV AWG during the impulse formation from high currents. The second element is the coupling capacitor (C_b), which protects the impulse generator from the HV AWG test source by blocking low-frequency waveforms. Instead of the coupling capacitor, it is possible to use a spark gap as a protective element. However, a capacitor offers more reliable operation compared to the spark gap [39]. Note that the design recommendations of the two additional parameters above are common for both traditional and integrated hybrid circuits. Moreover, the source capacitor (C_s) is added in the integrated hybrid circuit, which helps to maintain the voltage across the split dc link capacitor (C_{dc}) during the impulse formation.

The design of the source capacitor can be derived from the Marx generator design guidelines [40]. However, it affects the dc side input of the MMC-based HV AWG. Hence, it is essential to study its effect on the regular operation of the MMC-based HV AWG. With these additional elements and the involved coupling of two circuits, the design of such an integrated hybrid circuit needs to be carefully done analytically, with a simulation model and experimental setup. For simplicity, the analytical study of the integrated hybrid circuit is divided into three parts, i.e., the Marx generator side, MMC side, and the coupled circuits, and each part is elaborated in the following sections.

A. FROM MARX GENERATOR SIDE
Fig. 12 shows the schematic of the equivalent Marx generator circuit adapted from the integrated hybrid circuit. Here, the dc side input capacitor (C_1) is a series combination of two capacitors C_s and C_{dc} and the load capacitor (C_2) is also a
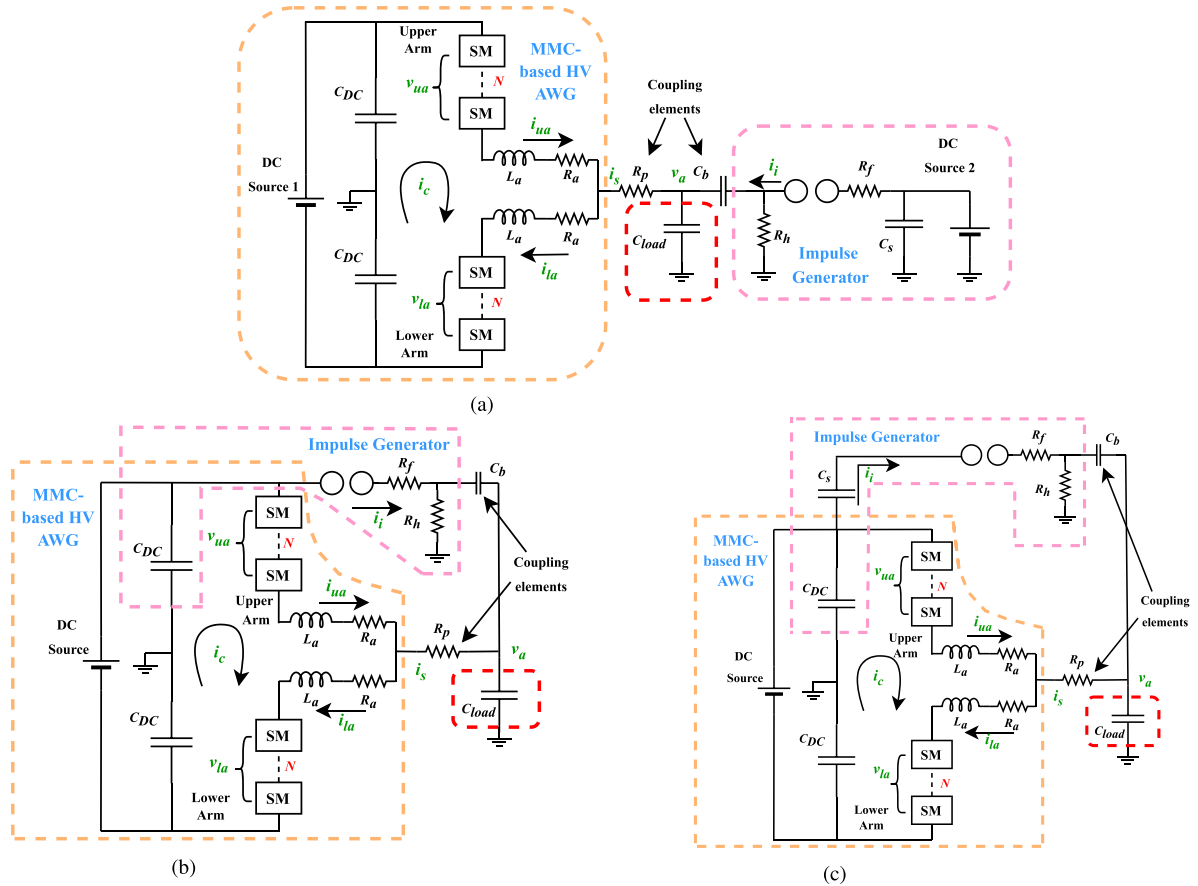
FIGURE 11. MMC-based HV AWG to generate the LI waveform. (a) Traditional superimposed circuit. (b) Integrated hybrid circuit 1. (c) Integrated hybrid circuit 2.
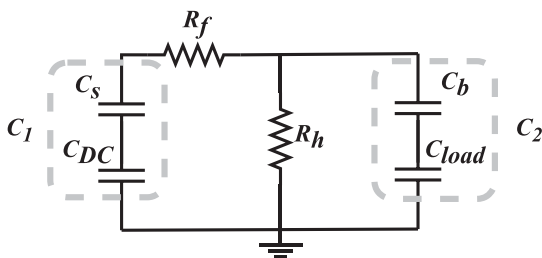

FIGURE 12. Equivalent Marx generator circuit.

FIGURE 13. Impulse formation.

series combination of two capacitors C_b and C_{load}. In this circuit, the impulse waveform is formed by subtracting one exponential function from another, as shown in Fig. 13. Mathematically, the impulse waveform is represented in (1), where the relationship of the circuit parameters (R_f, R_h, C_1, and C_2) to the time constants (α_1 and α_2) is shown from (2) to (5) [40]. The first exponential function ($e^{-\alpha_1 t}$) dictates the tail time of the impulse, and the second exponential function ($e^{-\alpha_2 t}$) decides the front time of the impulse. The rise time and the tail time of the impulse can be altered using the front resistor (R_f) and the tail resistor (R_h), respectively. Here, V_m is the magnitude of both of the exponential functions, and the V_p is

the peak amplitude of the obtained impulse waveform.

$$v_i(t) = V_m \left(e^{-\alpha_1 t} - e^{-\alpha_2 t} \right) \tag{1}$$

$$\alpha_1, \alpha_2 = \frac{a}{2} \mp \sqrt{\left(\frac{a}{2}\right)^2 - b} \tag{2}$$

$$a = \frac{1}{R_f C_1} + \frac{1}{R_f C_2} + \frac{1}{R_h C_1} \tag{3}$$

TABLE 2. Relationship of Time Constants of Impulse Waveforms to α_1 and α_2

Impulse Waveform	$1/\alpha_1$ (µs)	$1/\alpha_2$ (µs)
Lightning Impulse (1.2 µs/50 µs)	68.2	0.405
Switching Impulse (250 µs/2500 µs)	3155	62.5

$$b = \frac{1}{R_f R_h C_1 C_2} \quad (4)$$

$$k = R_f C_2 \quad (5)$$

$$V_m = \frac{V_0}{k(\alpha_2 - \alpha_1)}. \quad (6)$$

Though it is evident that the time constants (α_1 and α_2) in the exponential functions dictate the rise time and tail time of the impulse waveforms, the relationship is irrational, and its relationship is computed numerically, as done in [40]. Table 2 shows the relationship between the most common impulse waveforms in the HV testing. Based on these values, the front resistor and tail resistor can be calculated from (7) and (8) for the given values of capacitances (C_1 and C_2). The square-root term must exceed zero to obtain real values of the front and tail resistors. Hence, this puts a maximum condition on the ratio of C_1 and C_2 capacitors for real values of front and tail resistors, and it is shown in (9).

$$R_f = \frac{1}{2C_1}\left[\left(\frac{1}{\alpha_1} + \frac{1}{\alpha_2}\right)\right.$$
$$\left. - \sqrt{\left(\frac{1}{\alpha_1} + \frac{1}{\alpha_2}\right)^2 - \frac{4(C_1 + C_2)}{\alpha_1\alpha_2 C_2}}\right] \quad (7)$$

$$R_h = \frac{1}{2(C_1 + C_2)}\left[\left(\frac{1}{\alpha_1} + \frac{1}{\alpha_2}\right)\right.$$
$$\left. + \sqrt{\left(\frac{1}{\alpha_1} + \frac{1}{\alpha_2}\right)^2 - \frac{4(C_1 + C_2)}{\alpha_1\alpha_2 C_2}}\right] \quad (8)$$

$$\frac{C_1}{C_2} \le \frac{(\alpha_1 - \alpha_2)^2}{4\alpha_1\alpha_2}. \quad (9)$$

The most important criterion for creating design guidelines for the Marx generator is its voltage efficiency (η) of the generated impulse waveform. Fig. 13 makes it clear that the peak of the impulse waveform (V_p) will always be less than the charged voltage (V_m) of the input capacitor. However, it is possible to obtain a higher voltage by having the Marx generator with multiple stages. Here, the voltage efficiency (η) is defined as the ratio of V_p to V_m for the single-stage Marx generator. The magnitude of V_p can be obtained by finding the maxima of expression (1), and this leads to the efficiency expressions, as shown in (10) [40]. If $C_1 > C_2$ and $\alpha_2 >> \alpha_1$, the efficiency expression can be simplified, and it is shown in (11). This means that the ratio of C_1 and C_2 should be as large as possible to obtain HV efficiency. However, it should be less than the value calculated in (9) to obtain the real values of the
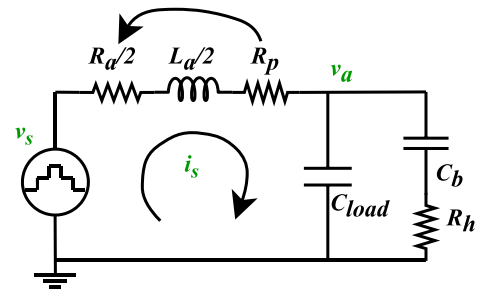
FIGURE 14. MMC side.

front and tail resistors for the given impulse waveform

$$\eta = \frac{(\alpha_2/\alpha_1)^{-}[\alpha_2/(\alpha_1 - \alpha_2)] - (\alpha_2/\alpha_1)^{-}[\alpha_2/(\alpha_2 - \alpha_1)]}{k(\alpha_2 - \alpha_1)} \quad (10)$$

$$\eta \approx \frac{1}{1 + (C_2/C_1)}. \quad (11)$$

B. FROM MMC SIDE

Considering the complex topology of MMC, it is essential to simplify the MMC circuit into an output current circuit and a circulating current circuit [4], [41] to study its coupling with the Marx generator. Here, the output current circuit dictates the waveform generation capability of MMC, and it is adapted when integrated with the Marx generation in Fig. 14. Apart from the usual output current circuit (v_s, R_a, L_a, and C_{load}), it has three additional elements, which are the parallel resistor (R_p), the coupling capacitor C_b, and the tail resistor R_h. All three are affecting the regular operation of the MMC-based AWG. Hence, their selection must consider the following three conditions.

1) The transient current is limited within the permitted range of the switches and other passive elements during the superposition of the impulse waveform.
2) The continuous arm current values need to be less than 5 A considering the rating of the designed switches.
3) The output voltage should not be dropped more than 1% due to the increased load to the MMC.
4) The normal operation of MMC needs to be restored, like balancing SM capacitor voltages and quality of output voltage waveform.

As explained earlier, the parallel resistor (R_p) is added before the load capacitor to protect the MMC from high transient currents generated when the impulse is superimposed on the arbitrary waveform. However, the equivalent circuit from Fig. 14 shows that the parallel resistor is in series with the arm resistor (R_a). Instead of adding a separate resistor, the arm resistors can be used to protect the MMC from transients generated during impulse formation. This reduces the requirement for an additional HV resistor. Hence, the arm resistor, apart from damping the resonance in the MMC-based AWG, is designed to limit the arm current transient that occurred due to the sudden change in the output voltage (v_a) during the

superposition of LI. As per the transfer function of the output current circuit of the MMC from Fig. 14, the minimum value of R_a to avoid undesired oscillations is defined in (12) [4]. It considers only the load capacitance instead of the series connection of two capacitances, as shown in Fig. 14 since the former case is more severe and needs a higher value of R_a to avoid oscillations during the impulse formation. Second, the resistance limits the peak current, and its magnitude can be estimated using the following expression (13). Additionally, the large arm inductor value reduces the di/dt on the switches, as shown in (14).

$$R_a \geq \sqrt{\left(\frac{8L_a}{C_{\text{load}}}\right)} \qquad (12)$$

$$I_{au,l} = \frac{V_p}{R_a} \qquad (13)$$

$$L_a = V_p \Bigg/ \left(\frac{i_{au,l}}{t}\right). \qquad (14)$$

The effect of the added load (C_b and R_h) on the MMC can be studied by finding its transfer function, and it is shown in (15)–(17). This transfer function clearly shows that the load has changed the typical second-order low-pass filter with two poles to a system with three poles and one zero. From the bode plot of this transfer function, the magnitude at the reference frequency of the MMC should be checked so that the voltage drop across the load of the MMC can be determined. Moreover, this added load affects the continuous arm current flowing through the MMC. The value of the coupling capacitor should be much higher than the load capacitor to obtain a higher voltage drop across C_{load} compared to C_b. However, it can overload the MMC, affecting the output voltage peak and drawing excessive current from the MMC. Assuming the value of C_b is much larger than C_{load}, the value of the coupling capacitor dictates the current flowing from the arm current ($I_{u,l} = V_a w C_b/2$). This current consumption should be kept within 5 A, considering the design specification of the test source. Generally, the chosen value of R_h is significantly less compared to the impedance of the capacitor.

$$\frac{V_a[s]}{V_s[s]} = \frac{2(C_b R_h s + 1)}{C_b C_l L_a R_h s^3 + ps^2 + qs + 2} \qquad (15)$$

$$p = ((C_{\text{load}} R_a R_h + L_a)C_b + C_{\text{load}} L_a) \qquad (16)$$

$$q = ((R_a + 2R_h)C_b + C_{\text{load}} R_a). \qquad (17)$$

The equivalent load of the MMC-based HV AWG is capacitive. Hence, there is no significant active power transfer in the MMC, with the average circulating current being zero [4]. Additionally, the output current requirement is not high (less than 5 A). Hence, the SM capacitor voltage balancing can be maintained with the phase shift carrier (PSC) modulation technique since it inherently uses the SMs evenly [42]. A similar principle is applied in this case since the value of the tail resistor is low.
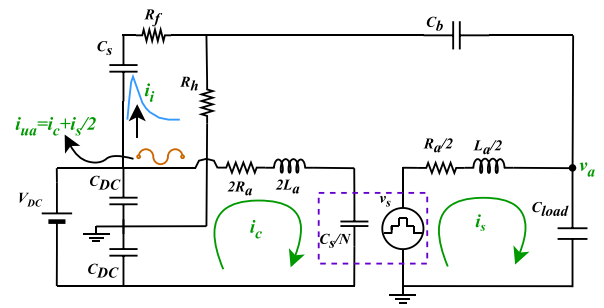

FIGURE 15. Coupling with integrated hybrid circuit.

C. COUPLED CIRCUIT

Fig. 15 shows the output current circuit and circulating current circuit of the MMC together with the Marx generator circuit and the coupling elements. The coupled circuit is analyzed from the dc side in the following sections. The Marx generator circuit design is revisited while considering the influence of the MMC branch ($L_a/2$ and $R_a/2$).

1) INPUT DC SIDE

The input dc side is the same for the two test sources for the integrated hybrid circuit. Hence, it is essential to look into the design of the dc link capacitors (C_{dc}) and the source capacitor (C_s). The dc link capacitance value should be as large as possible since it maintains the dc link voltage and generates proper bipolar waveforms without any offset in the MMC output voltage. However, as the dc link voltage increases, it is hard to obtain capacitors with more than a few hundred nanofarads commercially. These dc link capacitors provide the continuous arm currents ($i_{ua} = i_c + i_s/2 \approx i_s/2$) for the MMC, and it acts as a dc source to charge the Marx generator capacitor (C_s) with the impulse current (i_i). The value of this dc link capacitor can be decided based on the allowed voltage ripple due to the continuous MMC arm current (dv_1) in (18) and due to the very steep impulse (dv_2) in (20). The value of C_s should be chosen based on the ratio required for the better efficiency of the Marx generator, as shown in (9).

$$C_{\text{dc}} = \frac{1}{4\pi f dv_1} \frac{I_s}{2} \qquad (18)$$

$$I_s = m_a V_{\text{dc}} \pi f C_b \qquad (19)$$

$$C_{\text{dc}} = \frac{1}{dv_2} \int_0^{500\,\mu s} i_i \, dt. \qquad (20)$$

2) MARX GENERATOR WITH MMC

Fig. 15 shows the complete coupled circuit where the MMC branch ($L_a/2$ and $R_a/2$) is connected parallel to the load capacitor (C_{load}). This inductive load changes the behavior of impulses generated with the hybrid circuit of the MMC and the Marx generator. Note that the switching element (v_s) of the output current circuit is not considered in this analysis since it does not affect the dynamics of the Marx generator working in
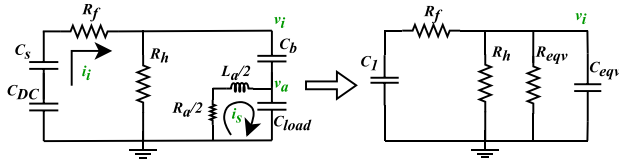
FIGURE 16. Updated Marx generator circuit with MMC.

FIGURE 17. LI waveform when generated from integrated hybrid circuit.

μs range and assuming the superposition principle of circuit analysis. Generally, the superimposed circuit discussed in [3] and [5] does not have this effect since the transformer or HVdc source has a large impedance, reducing its effect on the Marx generator. However, the arm inductor present in the MMC is finite, and it cannot be increased unlimitedly since it decides the output voltage characteristics of the MMC.

Though the equations from (1) to (11) give an excellent understanding of the Marx generator, it is important to analyze the updated circuit under the influence of the MMC branch, as shown in Fig. 16. The influence of the added MMC branch can be studied by calculating the equivalent parallel resistor (R_{eq}) and equivalent load capacitor (C_{eq}) for a particular frequency considering the impulse rise time or tail time from (21) and (22). The equivalent circuit can allow using the same equations to determine the front and tail resistors, as shown in (12) and (13) with updated Marx generator parameters

$$R_{eq} = \left(C_b^2 L_a^2 \, w^4 + 2C_b C_{load} L_a^2 \, w^4 + C_{load}^2 L_a^2 \, w^4 \right.$$
$$+ C_b^2 R_a^2 \, w^2 + 2C_b C_{load} R_a^2 \, w^2 + C_{load}^2 R_a^2 \, w^2$$
$$\left. - 4C_b L_a w^2 - 4C_{load} L_a w^2 + 4\right)/2C_b^2 R_a w^2 \quad (21)$$

$$C_{eq} = \left(C_b \left(C_b C_{load} L_a^2 \, w^4 + C_{load}^2 L_a^2 \, w^4 + C_b C_{load} R_a^2 \, w^2 \right.\right.$$
$$\left.+ C_{load}^2 R_a^2 \, w^2 - 2C_b L_a w^2 - 4C_{load} L_a w^2 + 4\right)\right)$$
$$/\left(C_b^2 L_a^2 \, w^4 + 2C_b C_{load} L_a^2 \, w^4 + C_{load}^2 L_a^2 \, w^4 \right.$$
$$+ C_b^2 R_a^2 \, w^2 + 2C_b C_{load} R_a^2 \, w^2$$
$$\left.+ C_{load}^2 R_a^2 \, w^2 - 4C_b L_a w^2 - 4C_{load} L_a w^2 + 4\right). \quad (22)$$

The equivalent circuit mentioned above gives the correct impulse waveform across the equivalent load (R_{eq} & C_{eq}) and not across the actual load. Hence, the voltage across the actual load (v_a) needs to be derived from the voltage across the equivalent load (v_i). The voltage across the actual load is derived first in the Laplace domain and then in the time domain from (23) to (27). Here, it is important to highlight that the time domain equation in (26) has another exponential term with α_3 time constant, and its value is dictated by the MMC parameters (R_a and L_a) and load parameters (C_{load} and C_b). Hence, the relation between time constants and impulse parameters shown in Table 2 is not valid anymore. Depending upon the MMC parameters and load parameters, the required α_1 and α_2 will differ, ultimately changing the choice of R_f
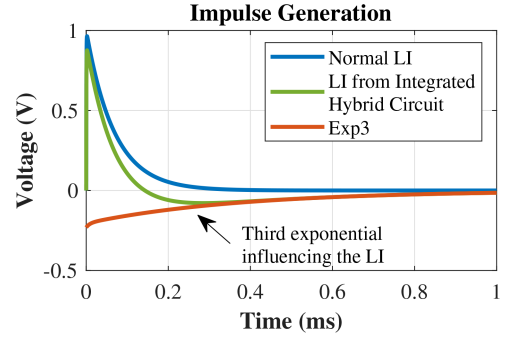
and R_h

$$V_a[s] = \frac{\left(\frac{R_a+sL_a}{2}\right) \| \left(\frac{1}{sC_{load}}\right)}{\left(\frac{R_a+sL_a}{2}\right) \| \left(\frac{1}{sC_{load}}\right) + \frac{1}{sC_b}} V_i[s]$$

$$= \frac{s^2 c + sd}{s^2 + sa_2 + b_2} V_i[s]$$

$$= \frac{s^2 c + sd}{s^2 + sa_2 + b_2} \left(\frac{Vm}{s+\alpha_1} - \frac{Vm}{s+\alpha_2}\right) \quad (23)$$

$$a_2 = \frac{R_a}{L_a}; b_2 = \frac{2}{L_a(C_b + C_{load})} \quad (24)$$

$$c = \frac{C_b}{(C_b + C_{load})}; d = \frac{R_a C_b}{L_a(C_b + C_{load})} \quad (25)$$

$$v_a(t) = \mathscr{L}^{-1}\left[\frac{s^2 c + sd}{s^2 + sa_2 + b_2}\left(\frac{Vm}{s+\alpha_1} - \frac{Vm}{s+\alpha_2}\right)\right]$$

$$= V_{m1}e^{-\alpha_1 t} - V_{m2}e^{-\alpha_2 t} - V_{m3}e^{-\alpha_3 t} \quad (26)$$

$$\alpha_3 = \frac{a_2}{2} - \sqrt{\left(\frac{a_2}{2}\right)^2 - b_2} \quad (27)$$

$$V_{m1} = \frac{-(\alpha_1 c - d)\alpha_1}{a_2 \alpha_1 - \alpha_1^2 - b_2}; V_{m2} = \frac{(\alpha_2 c - d)\alpha_2}{a_2 \alpha_2 - \alpha_2^2 - b_2} \quad (28)$$

$$V_{m3} \approx$$

$$\frac{(\alpha_1 - \alpha_2)(a_2\alpha_1\alpha_2 c - \alpha_1\alpha_2 d - \alpha_1 b_2 c - \alpha_2 b_2 c + b_2 \, d)}{(a_2\alpha_2 - \alpha_2^2 - b_2)(a_2\alpha_1 - \alpha_1^2 - b_2)}. \quad (29)$$

Fig. 17 shows the influence of the third exponential function on LI generation with circuit parameters as $R_a = 700\,\Omega$, $L_a = 6\,\text{mH}$, $C_b = 1\,\mu\text{F}$, and $C_{load} = 100\,\text{nF}$. Though the magnitude of the exponential term with α_3 time constant is not high, it impacts the tail time of the LI by reducing its value, and it adds a slight negative overshoot to the LI. Since the time constant of the third exponential function is much higher than the rise time of the impulse, it does not affect it. Hence, it is crucial to choose the MMC and load parameters so that rise time is not affected. Additionally, this third exponential limits how much tail time one can obtain with the given MMC and load parameters. For example, the time constant of the third
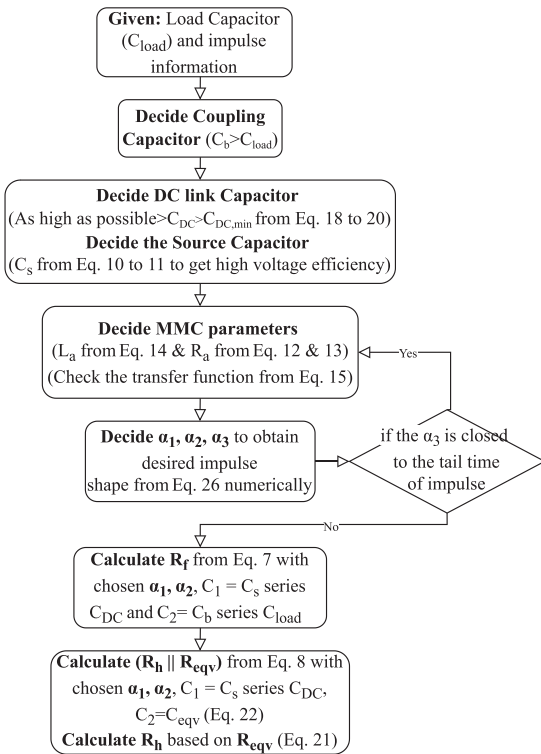
FIGURE 18. Parameter design procedure for the integrated hybrid circuit.

FIGURE 19. Integrated hybrid circuit for negative impulse generation.

FIGURE 20. Scaled down experimental setup.

exponential with the above-mentioned circuit parameters is 376 µs, and it is already not possible to obtain a tail time of more than 130 µs. The increase in the R_h has little influence on the tail time after this limit. It is important to choose the arm resistor that damps the resonance properly as per (12) for the above-derived equations to be valid. Fig. 18 summarizes a stepwise procedure for choosing the system parameters of the integrated hybrid circuit.

D. NEGATIVE IMPULSE
Generally, in the traditional Marx generator circuit, the negative impulse is generated by charging the input side capacitor to a negative voltage [16]. In the integrated hybrid circuit, the negative impulse is generated using the bottom dc link capacitor since it is negatively charged. The schematic of an integrated hybrid with negative impulse capability is shown in Fig. 19. Physically, the source capacitor's power connection must be changed from the +dc side to the -dc side capacitor. Moreover, the current direction is reversed since the negative impulse will generate current to flow from the load to the source. The other working principle of the integrated hybrid circuit remains the same as the positive impulse circuit with the current reversal.

V. SIMULATION AND EXPERIMENTAL RESULTS
The concept of the integrated hybrid circuit and the above-discussed analysis are validated with MATLAB-Simulink simulations and experimental results with a scaled-down prototype. The output voltage of 100 kV is scaled down to 150 V,
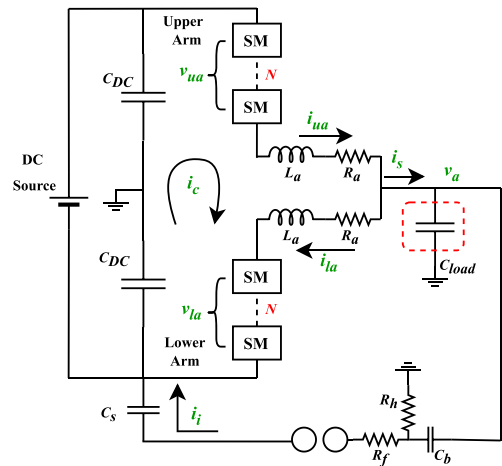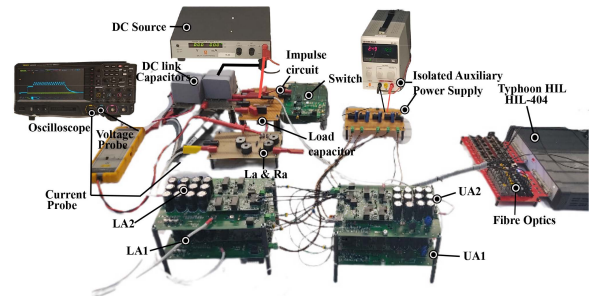
where the dc link voltage is 300 V with two submodules per arm. The 10 nF load capacitor is a worst-case scenario for LI waveform generation. However, for the scaled-down prototype, a higher value of the load capacitor of 100 nF is chosen to demonstrate the design of the integrated hybrid circuit since few submodules are present. For the given load capacitor, a coupling capacitor of 1 µF is used to get 90% of the impulse voltage across the load. The dc link capacitors for the Marx generator circuit are fixed to a significantly high value of 220 µF. For the source capacitor, 1.1 µF is chosen to obtain the voltage efficiency as high as 92% as per (11). Since there is a voltage drop across the coupling capacitor, the obtained efficiency will be around 82%. For the MMC, an arm inductance of 6 mH is selected, which imposes the arm resistor to be more than 698 Ω for an overdamped system. With the availability of a resistor in the ESP lab of TU Delft, an arm resistor of 750 Ω is added in the MMC to damp oscillations and to limit the transient in the arm current.

By following the procedure summarized in Fig. 18, the front resistor and tail resistor are calculated to be 5.1 and 79.7 Ω, respectively. However, based on the availability of resistors, the closest values of 5.45 and 76.7 Ω are prepared for the hardware. These system parameters are summarized in Table 3. Additionally, Fig. 20 shows the scaled-down prototype used for demonstrating the experimental results. It is
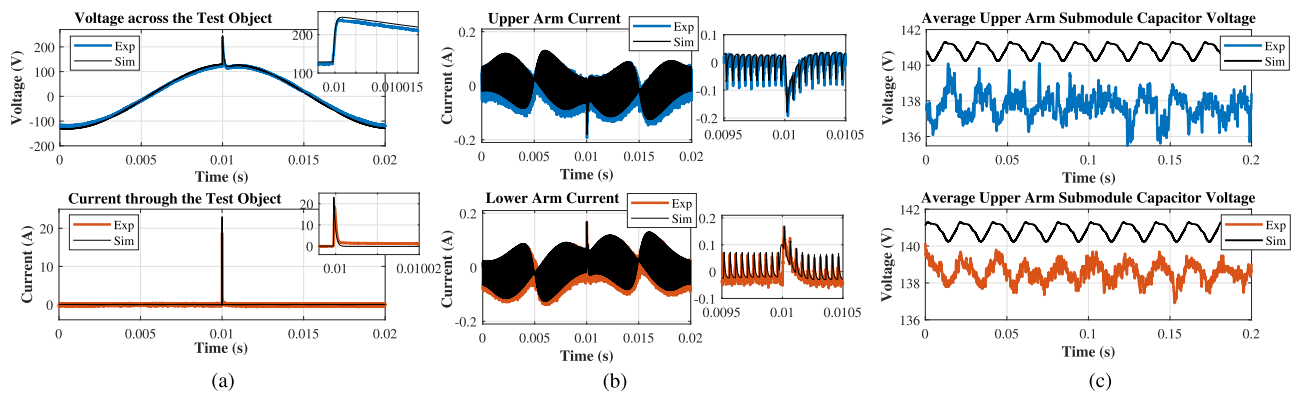
FIGURE 21. Positive LI superimposed on 50 Hz Sinusoidal Waveform. (a) Output characteristics. (b) Arm currents. (c) Submodule capacitor voltages.

TABLE 3. System Parameters of the Scaled Down Prototype

No.	Description	Label	Value
1.	DC link Voltage	V_{DC}	300 V
2.	Output Voltage	V_a	150 V
3.	Number of Submodules	N	2
4.	Modulation Index	m_a	0.9
5.	Submodule Capacitance	C_s	75 μF
6.	Arm Resistor	R_a	750 Ω
7.	Arm Inductor	L_a	6 mH
8.	Load Capacitor	C_{load}	100 nF
9.	Coupling Capacitor	C_b	1 μF
10.	DC link Capacitor	C_{DC}	220 μF
11.	Source Capacitor	C_s	1.1 μF
12.	Front Resistor	R_f	5.45 Ω
13.	Tail Resistor	R_h	76.7 Ω
14.	Switching Frequency	F_s	10.004 kHz
15.	Sampling Frequency	F_{samp}	50 kHz

TABLE 4. System Parameters of the HV Simulation Model

No.	Description	Label	Value
1.	DC link Voltage	V_{DC}	200 kV
2.	Output Voltage	V_a	100 kV
3.	Number of Submodules	N	67
4.	Modulation Index	m_a	0.9
5.	Submodule Capacitance	C_s	75 μF
6.	Arm Resistor	R_a	5 kΩ
7.	Arm Inductor	L_a	9 mH
6.	Load Capacitor	C_{load}	10 nF
8.	Coupling Capacitor	C_b	100 nF
9.	DC link Capacitor	C_{DC}	5 μF
10.	Source Capacitor	C_s	100 nF
11.	Front Resistor	R_f	51 Ω
12.	Tail Resistor	R_h	1318 Ω
13.	Tail Resistor	R_h	76.7 Ω
14.	Switching Frequency	F_s	50.004 kHz
15.	Sampling Frequency	F_{samp}	10 MHz

essential to highlight that all components of the Marx generator circuit are connected with the least possible wiring to avoid stray inductance, limiting the overshoot in the LI [34]. Also, a discrete TO-247 SiC MOSFET (H090) is implemented instead of a spark gap to demonstrate the idea of the integrated hybrid circuit. The chosen switching frequency for the MMC is much higher to remove all the switching harmonics since

low submodules per arm are present. All selected parameters are displayed in Table 3.

Fig. 21 showcases the LI superimposed on a 50 Hz sinusoidal waveform where the MATLAB-Simulink simulation results match well with the experimental results. Here, Fig. 21(a) displays the output voltage and current. The LI is superimposed on the sinusoidal waveform at 0.01 s, where the current through the test object is raised as high as 17 A in the experimental work to 22 A in the simulation results. The amount of current is reduced in the experiment considering the higher resistance and non-ideal nature of switching. The rise time and tail time of the obtained LI are 1.0 and 48 μs, respectively. The rise time and tail time are calculated based on the IEC standard (IEC60060-1) [6], and the obtained values are within the tolerances mentioned in the standard. Since the implemented tail resistor is slightly less than the designed values, the obtained tail time has a small error.

Additionally, the magnitude of LI is 115 V, which gives a voltage efficiency of 77%. This value is less than the designed value of 82%, considering the efficiency estimation is done with an approximate formula. Fig. 21(b) shows the arm currents and the transient current occurring at the superposition of impulse is well within the limit of the switches, and the peak of the transient current is the same as that of the estimate in (13). Lastly, Fig. 21(c) shows the average submodule capacitor voltages. The ripple waveform matches well from the simulation to the experimental results with an offset in their average voltages. It can be attributed to the higher arm resistor in the experiments. In this figure, the LI is superimposed on the positive peak of the sinusoidal. However, the time instant where the impulse is superimposed can be varied by changing the offset of the gate pulse sent to the switch.

Fig. 22 shows the positive LI superimposed on three other arbitrary wave shapes, where the output voltage, output current, and the submodule capacitor voltages are shown. First, Fig. 22(a) displays the superposition of positive LI on the negative dc waveform for the duration of 2 ms. The second waveform in Fig. 22(b) is the transient waveform containing 50 Hz sinusoidal and higher harmonics. At last, Fig. 22(c) shows the unipolar complex waveform with LI at the 0.02 s
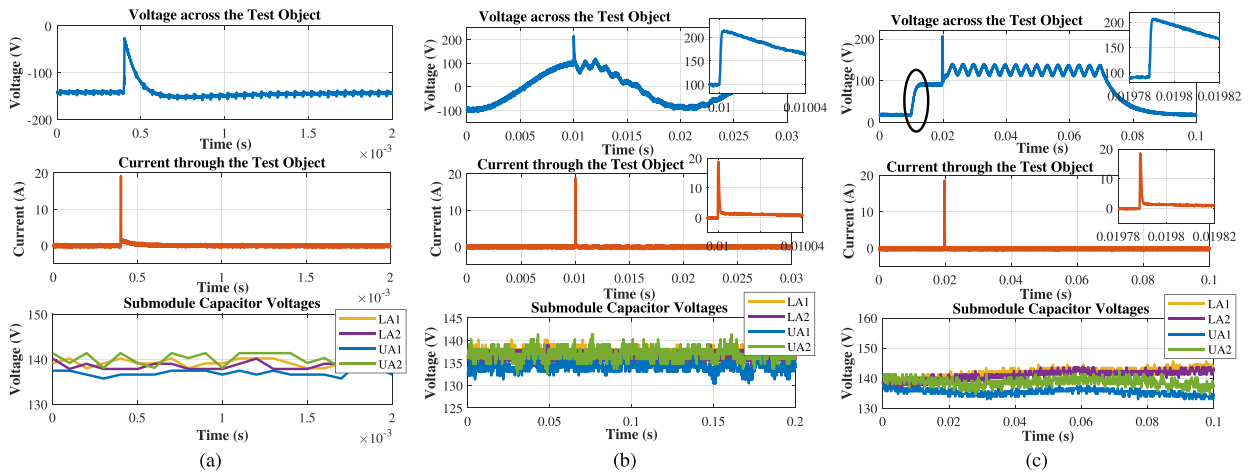
FIGURE 22. Positive LI superimposed on (a) negative dc, (b) 50 Hz Sinusoidal and higher harmonics, and (c) unipolar complex waveform.
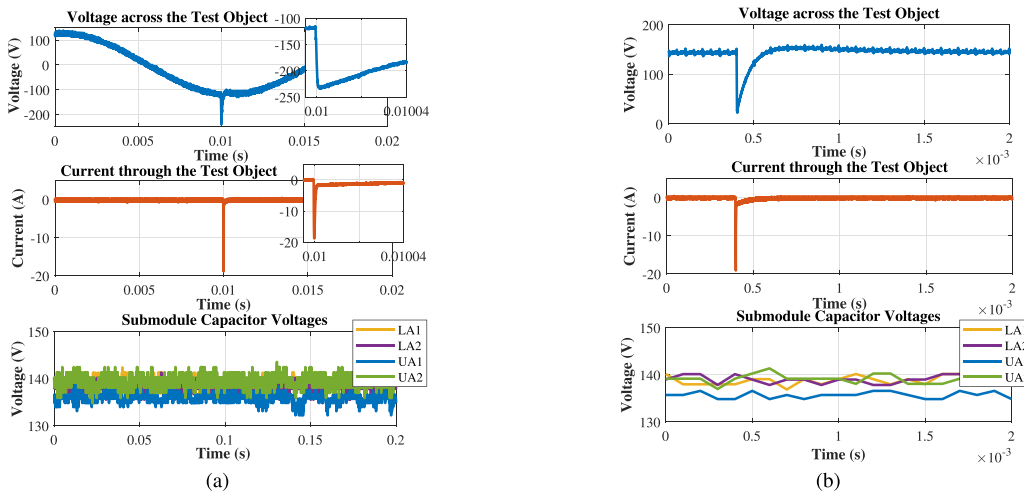

FIGURE 23. Negative LI superimposed on (a) 50 Hz sinusoidal and (b) negative dc waveform.

time instant. For the unipolar waveform like in Fig. 22(a) and (c), the submodule capacitor voltages are shown only for the time interval of the output voltage waveform. These waveforms are not continuously generated like sinusoidal, but they are generated as a single shot. Because the submodule capacitor voltages start to get unbalanced with its continuous generation, mainly due to just two submodules per arm. The generation of unipolar waveforms needs further work to invent a proper control methodology using Full Bridge topology, which is out of this article's scope. Fig. 23 displays the results when negative LI is superimposed on sinusoidal and dc waveforms. As discussed in the last section, the working principle of the negative impulse generation is the same where the current direction is reversed.

VI. HV SIMULATION RESULTS

This section demonstrates the performance of the integrated hybrid circuit with 200 kV DC link voltage and 10 nF of load capacitor. This study is critical to verify if it is possible

to choose system parameters at HV and achieve the superposition of LI without affecting the MMC. Similar to the scaled-down prototype, the coupling capacitor is first chosen as 100 nF considering the 90% voltage drop across the load capacitor. The dc link capacitor at HV can not be very high, and it is chosen based on (18)–(20) to keep the voltage ripple within 2%. The additional source capacitor is chosen to be 500 nF to obtain the voltage efficiency high in the range of 95%. For HV MMC, the arm inductance and the arm resistor are chosen to be 9 mH and 5 kΩ. For the LI generation, the front and tail resistors are calculated by following the flowchart summarized in Fig. 18, and they are 51 and 1318 Ω. Note that the selected resistors with high values are available commercially for this specific application of the impulse generation in [43]. All the system parameters used for performing HV simulations in MATLAB-Simulink are summarized in Table 4.

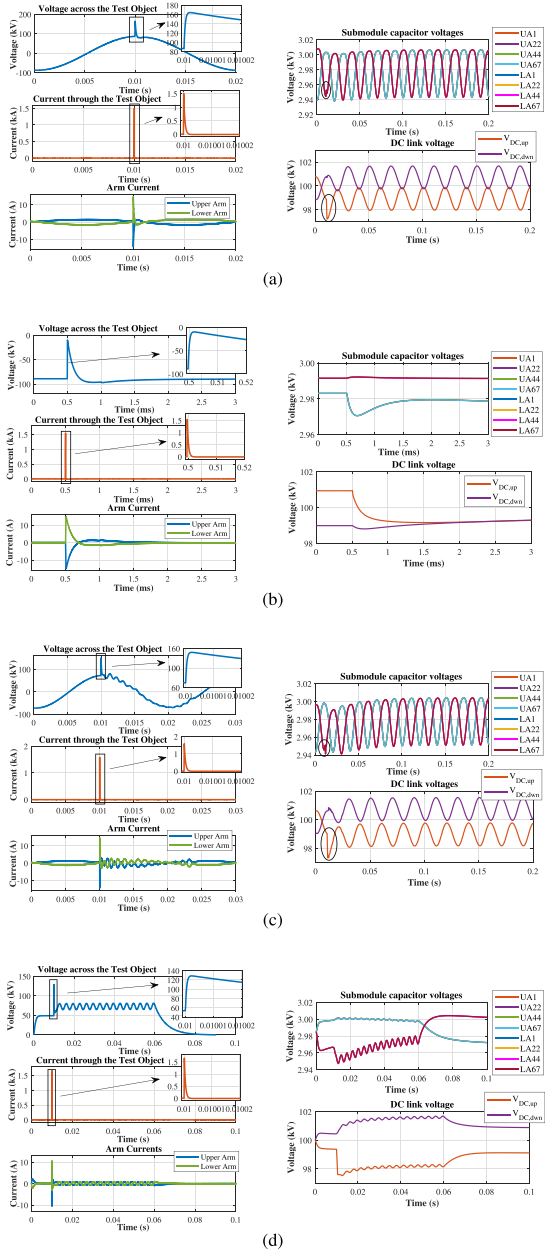The MATLAB-Simulink simulation results with the parameters mentioned above are shown in Figs. 24 and 25

FIGURE 24. Positive LI superimposed on (a) 50 Hz sinusoidal. (b) Negative DC. (c) 50 Hz sinusoidal and higher harmonics. (d) Unipolar complex waveform.

with positive and negative impulse generation. These figures include information about the output voltage, output current, arm currents, submodule capacitor voltages from the selected submodules (UA1, UA22, UA44, UA67, LA1, LA22, LA44, and LA67), and the voltage across the dc link capacitor voltage. It is essential to highlight that the choice of arm resistor is sufficient, and it limits the transient arm current to 13 A. Most semiconductor devices can handle a pulse current of 2–3 times higher than the rated values [14]. Even though this creates a large pulse voltage of 65 kV, it is possible to select the resistors rated for the peak value of
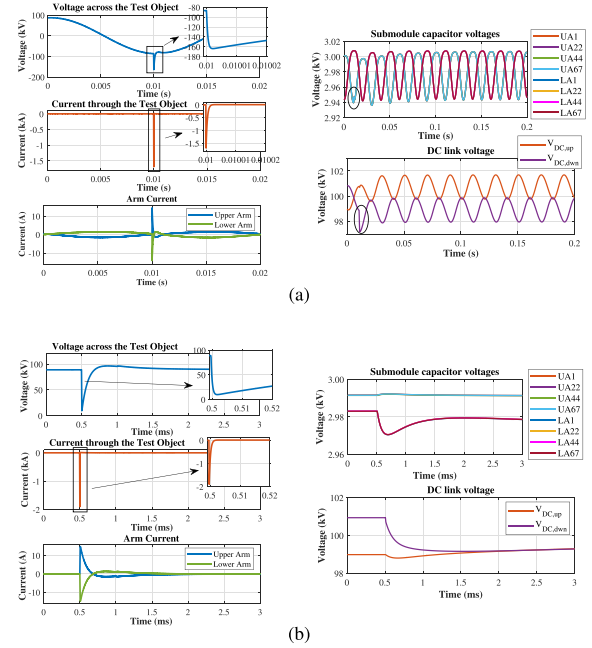

FIGURE 25. Negative LI superimposed on (a) 50 Hz sinusoidal. (b) Positive dc waveform.

voltage from the commercially available resistors [43]. Since the arm currents are limited during the superposition, their effect on the submodule capacitor voltages is limited for all wave shapes. Additionally, the submodule capacitor voltages are better balanced with dc and unipolar waveform with 67 submodules than two submodules. The generated LI has a rise and fall time of 1.2 and 50 μs since ideal switches and resistors are used. The obtained voltage efficiency is 77.2%, which is the typical efficiency value with the Marx generator circuit.

VII. CONCLUSION

This article introduces a new configuration combining the MMC-based HV AWG and the Marx generator to generate fast-rising waveforms successfully since the MMC-based HV AWG cannot generate them by themselves due to stringent requirements of switch current and issues with the jitter present in the switches. Among the three proposed configurations, the chosen integrated hybrid circuit is studied analytically concerning the Marx generator circuit from the MMC side and when they are coupled together. Interestingly, the finite values of the MMC arm inductor and arm resistor affect the Marx generator circuit and influence impulse formation by adding a third exponential function. This added impedance from the MMC deviates the experimentally obtained tail time from the standard analytical calculations of the Marx Generator and requires a new guideline for the tail resistor selection. This article provides an exhaustive summary of how to choose the tail resistor and its limitation of impulse formation. All discussed design guidelines are verified with a scaled-down hardware
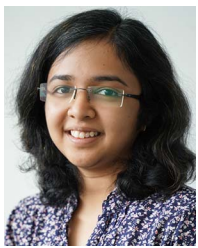
prototype and HV simulation results. It demonstrates that the designed system works well, giving a time-controllable LI waveform superimposed on different arbitrary wave shapes without the MMC getting affected by the impulse formation.

ACKNOWLEDGMENT

REFERENCES

[1] S. Mukherjee, Y.-J. Häfner, S. Nyberg, and M. Saltzer, "Cable overvoltage for MMC based VSC HVDC system: Interaction with converters," *CIGRE India J.*, vol. 7, no. 2, pp. 18–23, 2018.

[2] S. Alapti, K. Johansson, M. Sjoberg, M. Klang, A. Abbasi, and M. Saltzer, "Transient over voltage testing of cable systems in MMC-HVDC links: A concept study including verification," *CIGRE Paris Session*, B1-10514_2022, 2022.

[3] J. Wu, "Effects of transients on high voltage cable insulation," Ph.D. dissertation, Delft Univ. Technol., Delft, The Netherlands, 2020.

[4] D. A. Ganeshpure, T. B. Soeiro, M. G. Niasar, P. Vaessen, and P. Bauer, "Design trade-offs of modular multilevel converter-based arbitrary wave shape generator for conventional and unconventional high voltage testing," *IEEE Open J. Ind. Electron. Soc.*, vol. 2, pp. 584–605, 2021, doi: 10.1109/OJIES.2021.3125747.

[5] *High Voltage Direct Current (HVDC) Power Transmission*, IEC 62895, 2017.

[6] *High-Voltage Test Techniques-Part 1: General Definitions and Test Requirements*, IEC 60060-1, 2011.

[7] "Advanced energy–High voltage power amplifier products," Accessed: Dec. 13, 2020, [Online]. Available: https://www.advancedenergy.com/products/high-voltage-products/high-voltage-amplifiers/

[8] P. Mathew, M. G. Niasar, and P. Vaessen, "Design of high-frequency fast-rise pulse modulators for lifetime testing of dielectrics," *IEEE Trans. Dielectr. Electr. Insul.*, vol. 30, no. 6, pp. 2798–2808, Dec. 2023.

[9] "Internal test reports, KEMA Laboratories, Arnhem, Netherlands," Confidential, 2019.

[10] M. Hochberg et al., "A fast modular semiconductor-based marx generator for driving dynamic loads," *IEEE Plasma Sci.*, vol. 47, no. 1, pp. 627–634, Jan. 2019.

[11] L. Redondo, A. Kandratsyeu, M. Barnes, S. Calatroni, and W. Wuensch, "Solid-state marx generator for the compact linear collider breakdown studies," in *Proc. IEEE Int. Power Modulator High Voltage Conf.*, 2016, pp. 187–192.

[12] T. B. Soeiro, E. Mengotti, E. Bianda, and G. Ortiz, "Performance evaluation of the body-diode of SiC Mosfets under repetitive surge current operation," in *Proc. 45th Annu. Conf. IEEE Ind. Electron. Soc.*, 2019, pp. 5154–5159, doi: 10.1109/IECON.2019.8927774.

[13] S. Yin, Y. Gu, S. Deng, X. Xin, and G. Dai, "Comparative investigation of surge current capabilities of SI IGBT and SiC MOSFET for pulsed power application," *IEEE Plasma Sci.*, vol. 46, no. 8, pp. 2979–2984, Aug. 2018, doi: 10.1109/TPS.2018.2849778.

[14] D. A. Ganeshpure, A. P. Soundararajan, T. B. Soeiro, M. G. Niasar, P. Vaessen, and P. Bauer, "Comparison of pulse current capability of different switches for modular multilevel converter-based arbitrary wave shape generator used for dielectric testing of high voltage grid assets," in *Proc. 24th Eur. Conf. Power Electron. Appl.*, 2022, pp. 1–11.

[15] C. Davidson, J. Vodden, and J. Snazell, "A new test circuit for operational testing of HVDC valves," in *Proc. 15th IET Int. Conf. AC DC Power Transmiss.*, 2019, pp. 1–6.

[16] F. H. Kreuger, "Industrial high voltage Volume II: 4. Co-ordinating, 5. Measuring, 6. Testing," Delft Univ. Press, Delft, 1992.

[17] T. J. Blalock, "High-voltage testing: Man-made lightning at the 1939 world's fair [history]," *IEEE Power Energy Mag.*, vol. 8, no. 2, pp. 62–81, Mar./Apr. 2010, doi: 10.1109/MPE.2009.935480.

[18] *Voltage Characteristics of Electricity Supplied by Public Electricity Networks*, NEN-EN 50160, 2010.

[19] "Difference between current transformer (CT) & potential transformer (PT)," Accessed: May 31, 2021. [Online]. Available: https://circuitglobe.com/difference-between-current-transformer-ct-and-potential-transformer-pt.htm

[20] "Current transformer, how it works?," Accessed: May 25, 2021. [Online]. Available: https://electrical4u.com/current-transformer-ct-class-ratio-error-phase-angle-error-in-current-transformer/

[21] "Different types of transformers–Shell and core type transformer," Accessed: 2021. [Online]. Available: https://www.electricalengineeringinfo.com/2015/01/types-of-transformers-shell-type-transformer-core-type-transformer.html

[22] "4 Methods of medium-voltage circuit breaker design," Accessed: Apr. 24, 2021. [Online]. Available: https://testguy.net/content/245-4-Methods-of-Medium-Voltage-Breaker-Design

[23] "Construction of power transformer," Accessed: May 31, 2021. [Online]. Available: http://eee-resetsg.blogspot.com/2016/02/construction-of-power-transformer.html

[24] A. Shekhar et al., "Impact of DC voltage enhancement on partial discharges at semicon-dielectric interface," *Energies*, vol. 10, no. 12, 2017, Art. no. 1968.

[25] "Potential Transformers," Accessed: May 25, 2021. [Online]. Available: https://www.electricalclassroom.com/potential-transformer-voltage-pt/

[26] *High-Voltage Switchgear and Control Gear-Part 1: Common Specifications for ac Switchgear and Controlgear*, IEC 62271-1, 2017.

[27] *Power Cables With Extruded Insulation and Their Accessories for Rated Voltages from 1 kV (Um = 1,2 kV) up to 30 kV (Um = 36 kV) – Part 2: Cables for Rated Voltages from 6 kV (Um = 7,2 kV) up to 30 kV (Um = 36 kV)*, IEC 60502-2, 2014.

[28] *Power Transformers–Part 3: Insulation Levels, Dielectric Tests and External Clearances in Air*, IEC 60076-3, 2013.

[29] *Instrument Transformers-Part 6: Additional General Requirements for Low-Power Transformers (IEC 61869-6:2016, IDT)*, IEC 61869-6, 2016.

[30] "Twenpower medium-voltage XLPE cables, TKF Cable," Accessed: May 31, 2021. [Online]. Available: https://t3.lappcdn.com/fileadmin/DAM/Miltronic_Sweden/4_Servicecenter/2_Nedladdningscenter/TKF_Twenpower_Medium_Voltage.pdf

[31] A. Greenwood, *Electrical Transients in Power Systems*. 2nd edition, USA, 1991.

[32] F. Barakou, "Investigation of the impact of EHV underground power cables on the resonant and transient grid behavior," Ph.D. dissertation, Eindhoven Univ. Technol., Eindhoven, The Netherlands, 2018.

[33] "Electrical transient interaction between transformers and the power system–part 1: Expertise," JWG A2/C4.39, pp. 99–104, 2014.

[34] W. Hauschild et al., *High-Voltage Test and Measuring Techniques*, vol. 1. Berlin, Germany: Springer, 2014.

[35] K. Schon, *High Impulse Voltage and Current Measurement Techniques*. Berlin, Germany: Springer, 2013.

[36] W. Wang, X. Wang, J. He, Y. Liu, S. Li, and Y. Nie, "Electric stress and dielectric breakdown characteristics under high-frequency voltages with multi-harmonics in a solid-state transformer," *Int. J. Elect. Power Energy Syst.*, vol. 129, 2021, Art. no. 106861.

[37] M. G. Niasar, N. Taylor, H. Edin, and R. C. Kiiza, "Dielectric frequency response of oil-impregnated paper: The effect of partial discharges compared to other influences," *IEEE Trans. Dielectr. Electr. Insul.*, vol. 23, no. 3, pp. 1769–1777, Jun. 2016, doi: 10.1109/TDEI.2016.005169.

[38] T. Koltunowicz, G. Bajracharya, D. Djairam, and J. Smit, "Exploring the feasibility of an aging model for paper insulation based on the repetition frequency of transients," in *Proc. IEEE Int. Symp. Elect. Insul.*, 2010, pp. 1–5, doi: 10.1109/ELINSL.2010.5549773.

[39] A. Voß and M. Gamlin, "Superimposed impulse voltage testing on extruded DC-cables according to IEC 62895," in *Proc. Symp. Energieinnovation*, 2017.

[40] J. Kuffel and P. Kuffel, *High Voltage Engineering Fundamentals*. Amsterdam, Netherlands: Elsevier, 2000.

[41] K. Sharifabadi, L. Harnefors, H.-P. Nee, S. Norrga, and R. Teodorescu, *Design, Control, and Application of Modular Multilevel Converters for HVDC Transmission Systems*. Hoboken, NJ, USA: Wiley, 2016.

[42] W. van der Merwe, P. Hokayem, and L. Stepanova, "Analysis of the n-cell single phase MMC natural balancing mechanism," *IEEE Trans. Emerg. Sel. Topics Power Electron.*, vol. 2, no. 4, pp. 1149–1158, Dec. 2014, doi: 10.1109/JESTPE.2014.2346137.

[43] "High voltage resistors and pulsed power resistors," Accessed: Dec. 26, 2023. [Online]. Available: https://www.genvolt.com/files/Datasheets/2023Dec/RES100%20and%20RES200%20High%20Voltage%20Resistors%20Data%20Sheet%202021.pdf

DHANASHREE ASHOK GANESHPURE (Member, IEEE) received the bachelor's degree in electrical and electronics engineering from BITS Pilani University, Goa, India, in 2015, the master's degree *(cum laude)* in electrical power engineering and the Ph.D. degree in design of a high voltage arbitrary wave shape generator for dielectric testing from the Delft University of Technology, Delft, The Netherlands, in 2018, and 2024, respectively.

During her Ph.D., she focused on developing a power electronics-based HV test source to generate arbitrary wave shapes for unconventional and futuristic HV testing applications. Currently, she is with Shell, London, U.K. as an Electrical Engineer to facilitate the integration of various renewable energy sources into the grid using novel power electronics solutions.

THIAGO BATISTA SOEIRO (Senior Member, IEEE) received the B.S. (Hons.) and M.S. degrees in electrical engineering from the Federal University of Santa Catarina, Florianopolis, Brazil, in 2004 and 2007, respectively, and the Ph.D. degree in electrical engineering from the Swiss Federal Institute of Technology, Zurich, Switzerland, in 2012.

He was a Visiting Scholar with the Power Electronics and Energy Research Group, Concordia University, Montreal, QC, Canada, and with the Center for Power Electronics Systems, Blacksburg, VA, USA, respectively. From 2012 to 2013, he was a Researcher with the Power Electronics Institute, Federal University of Santa Catarina. From 2013 to 2018, he was a Senior Scientist with the Corporate Research Center, ABB Switzerland Ltd., Baden-Dattwil, Switzerland. From 2018 to 2022, he was an Associate Professor with the DC Systems, Energy Conversion and Storage Group, Delft University of Technology, Delft, The Netherlands. In 2022, he was with the Power Management and Distribution Section (TEC-EPM) for the European Space Research and Technology Centre, Noordwijk, The Netherlands. Since 2022, he has been a Full Professor for Power Electronics with the Power Electronics and EMC Group, University of Twente, Enschede, The Netherlands. His research interests include advanced high-power converters and dc system integration.

Dr. Soeiro was the recipient of the 2013 IEEE Industrial Electronics Society Best Conference Paper Award and the Best Paper Awards in the following IEEE conferences: International Conference on Power Electronics (ECCE Asia 2011), the International Conference on Industrial Technology (ICIT 2013), the Conference on Power Electronics and Applications EPE 2015 (ECCE Europe 2015), and the International Conference on Power Electronics and Motion Control 2020 and 2022 (PEMC 2020 and 2022).

MOHAMAD GHAFFARIAN NIASAR (Member, IEEE) was born in Tehran, Iran in 1984. He received the M.Sc. degree in electrical power engineering from the Sharif University of Technology, Tehran, Iran, in 2008, and Ph.D. degree in electrical engineering from the Royal Institute of Technology (KTH), Stockholm, Sweden, 2015.

He is currently an Assistant Professor with DC System, Energy Conversion & Storage group, Technical University of Delft, Delft, The Netherlands. His main research interests include aging of electrical insulation, HVdc insulation system, partial discharges, high frequency power transformers, power cables, and FEM modeling.

NITISH MILIND KULKARNI received the bachelor's degree (as a gold medalist) in electrical engineering from the Institute of Technology, Nirma University, Ahmedabad, India, in 2019 and the M.S. degree *(cum laude)* in electrical power engineering from the Delft University of Technology, Delft, The Netherlands, in 2022.

He is currently working as a High Voltage Systems Engineer with Prysmian Group Netherlands, Delft, The Netherlands.

PAVOL BAUER (Senior Member, IEEE) received master's degree in electrical engineering from the Technical University of Kosice, Košice, Slovakia, in 1985, and the Ph.D. degree from the Delft University of Technology, Delft, Netherlands, in 1995.

He is currently a Full Professor with the Department of Electrical Sustainable Energy, Delft University of Technology, Delft, The Netherlands, and the Head of DC Systems, Energy Conversion and Storage group. He is also Professor with Brno University of Technology, Brno, Czech Republic, Honorary Professor with Politehnica University Timisioira, Timisoara, Romania, where he obtained a honorary doctorate too. From 2002 to 2003, he was working partially with KEMA (DNV GL, Arnhem) on different projects related to power electronics applications in power systems. He published over 180 journal and 450 conference papers in his field (with H factor Google scholar 59, Web of Science 42), he is an author or co-author of eight books, holds ten international patents, and organized several tutorials at the international conferences. He has worked on many projects for industry concerning wind and wave energy, power electronic applications for power systems, such as Smarttrafo; HVdc systems, projects for smart cities such as PV charging of electric vehicles, PV and storage integration, contactless charging; and he participated in several Leonardo da Vinci, H2020 and Electric Mobility Europe EU projects as project partner (ELINA, INETELE, E-Pragmatic, Micact, Trolly 2.0, OSCD, P2P, Progressus, Tulip, Flow) and coordinator (PEMCWebLab.com-Edipe, SustEner, Eranet DCMICRO). His main research interest includes power electronics for charging of electric vehicles and dc grids.

Dr. Bauer is a former Chairman of Benelux IEEE Joint Industry Applications Society, Power Electronics and Power Engineering Society chapter, Chairman of the Power Electronics and Motion Control (PEMC) council, Chairman of Benelux IEEE Industrial Electronics chapter, Member of the Executive Committee of European Power Electronics Association (EPE), and also the Member of international steering committee at numerous conferences.

PETER VAESSEN (Member, IEEE) received the M.Sc. degree *(cum laude)* in electrical power engineering from Eindhoven Technical University, Eindhoven, The Netherlands, in 1985.

He joined KEMA (now a CESI brand) in 1985. In his career, he held research positions in the field of large power transformers and high voltage measurement & testing. He headed the Transmission & Distribution high voltage department and managed realization projects, among them construction of Dutch 400 kV substations and laboratory test facilities. As a Principal Consultant, he has 30 years experience in (U)HVdc technology and transmission & distribution grids with high shares of renewables. He is the Manager Innovations with CESI and actively involved in the technology strategy. He is a part-time Professor of Hybrid Transmission Systems with TU Delft, Delft, The Netherlands, where he teaches high voltage technology and HVdc and the Head of the High Voltage Technologies group of the ESE Department.

Mr. Vaessen is the Member of the board of the European Distributed Energy Resources Laboratories Association (DERlab) and a Member of several national and international working groups.